Ionizing properties of galaxies in JADES for a stellar mass complete sample: resolving the cosmic ionizing photon budget crisis at the Epoch of Reionization

C. Simmonds [1,2]★ S. Tacchella [1,2] K. Hainline,[3] B. D. Johnson,[4] D. Puskás,[1,2] B. Robertson,[5] W. M. Baker [1,2] R. Bhatawdekar [6] K. Boyett [7,8] A. J. Bunker,[9] P. A. Cargile,[4] S. Carniani,[10] J. Chevallard,[9] M. Curti,[11] E. Curtis-Lake,[12] Z. Ji,[3] G. C. Jones,[9] N. Kumari,[13] I. Laseter,[14] R. Maiolino,[1,2,15] M. V. Maseda,[14] P. Rinaldi,[3] A. Stoffers,[1,2] H. Übler,[1,2] N. C. Villanueva,[1,2] C. C. Williams,[16] C. Willott,[17] J. Witstok[1,2] and Y. Zhu[3]

[1]*The Kavli Institute for Cosmology (KICC), University of Cambridge, Madingley Road, Cambridge, CB3 0HA, UK*
[2]*Cavendish Laboratory, University of Cambridge, 19 JJ Thomson Avenue, Cambridge, CB3 0HE, UK*
[3]*Steward Observatory, University of Arizona, 933 N. Cherry Avenue, Tucson, AZ 85721, USA*
[4]*Center for Astrophysics | Harvard & Smithsonian, 60 Garden St, Cambridge, MA 02138, USA*
[5]*Department of Astronomy and Astrophysics University of California, Santa Cruz, 1156 High Street, Santa Cruz CA 96054, USA*
[6]*European Space Agency (ESA), European Space Astronomy Centre (ESAC), Camino Bajo del Castillo s/n, 28692 Villanueva de la Cañada, Madrid, Spain*
[7]*School of Physics, University of Melbourne, Parkville 3010, VIC, Australia*
[8]*ARC Centre of Excellence for All Sky Astrophysics in 3 Dimensions (ASTRO 3D), Canberra 2611, Australia*
[9]*Department of Physics, University of Oxford, Denys Wilkinson Building, Keble Road, Oxford OX1 3RH, UK*
[10]*Scuola Normale Superiore, Piazza dei Cavalieri 7, I-56126 Pisa, Italy*
[11]*European Southern Observatory, Karl-Schwarzschild-Strasse 2, 85748 Garching, Germany*
[12]*Centre for Astrophysics Research, Department of Physics, Astronomy and Mathematics, University of Hertfordshire, Hatfield AL10 9AB, UK*
[13]*AURA for European Space Agency, Space Telescope Science Institute, 3700 San Martin Drive. Baltimore, MD, 21210, USA*
[14]*Department of Astronomy, University of Wisconsin-Madison, 475 N. Charter St, Madison, WI 53706, USA*
[15]*Department of Physics and Astronomy, University College London, Gower Street, London WC1E 6BT, UK*
[16]*NSF's National Optical-Infrared Astronomy Research Laboratory, 950 North Cherry Avenue, Tucson, AZ 85719, USA*
[17]*NRC Herzberg, 5071 West Saanich Road, Victoria, BC V9E 2E7, Canada*

ABSTRACT

We use NIRCam imaging from the JWST Advanced Deep Extragalactic Survey (JADES) to study the ionizing properties of a sample of 14 652 galaxies at $3 \leq z_{\rm phot} \leq 9$, 90 per cent complete in stellar mass down to $\log(M_\star/[M_\odot]) \approx 7.5$. Out of the full sample, 1620 of the galaxies have spectroscopic redshift measurements from the literature. We use the spectral energy distribution fitting code Prospector to fit all available photometry and infer galaxy properties. We find a significantly milder evolution of the ionizing photon production efficiency ($\xi_{\rm ion}$) with redshift and UV magnitude than previously reported. Interestingly, we observe two distinct populations in $\xi_{\rm ion}$, distinguished by their burstiness (given by SFR_{10}/SFR_{100}). Both populations show the same evolution with z and $M_{\rm UV}$, but have a different $\xi_{\rm ion}$ normalization. We convolve the more representative $\log(\xi_{\rm ion}(z, M_{\rm UV}))$ relations (accounting for $\sim 97\%$ of the sample), with luminosity functions from literature, to place constraints on the cosmic ionizing photon budget. By combining our results, we find that one of our models can match the observational constraints from the Ly α forest at $z \lesssim 6$. We conclude that galaxies with $M_{\rm UV}$ between -16 and -20, adopting a reasonable escape fraction, can produce enough ionizing photons to ionize the Universe, without exceeding the required ionizing photon budget.

Key words: galaxies: evolution – galaxies: general – galaxies: high-redshift – dark ages, reionization, first stars.

1 INTRODUCTION

The Epoch of Reionization (EoR) is one of the major phase transitions of the Universe, when it went from being dark and neutral to highly ionized, allowing Lyman Continuum (Ly C; with energies above 13.6 eV) radiation to travel through the intergalactic medium (IGM). Observations place the end of this epoch at $z \sim 6$ (Becker et al. 2001; Fan et al. 2006; Yang et al. 2020), with some favouring a later reionization at $z \sim 5$ (Keating et al. 2020; Bosman et al. 2022; Zhu et al. 2024). There is a debate regarding which sources are the main responsible agents in ionizing the Universe. The community

★ E-mail: cs2210@cam.ac.uk

widely agrees that young massive stars within galaxies are key, since they produce copious amounts of ionizing photons, which might be able to escape the interstellar medium (ISM), and eventually ionize the IGM (Hassan et al. 2018; Rosdahl et al. 2018; Trebitsch, Volonteri & Dubois 2020). However, the nature of the galaxies that drive reionization: bright and massive, faint and low-mass, or a combination of them, is still uncertain (Finkelstein et al. 2019; Naidu et al. 2020; Robertson 2022; Yeh et al. 2023). Moreover, it is unclear how much active galactic nuclei (AGNs) contribute to reionization (Dayal et al. 2020; Maiolino et al. 2024a; Madau et al. 2024).

The stellar mass of galaxies has been seen to correlate with how efficiently ionizing photons are produced (Simmonds et al. 2024a). Simulations indicate that it also relates how these ionizing photons escape (Paardekooper, Khochfar & Dalla Vecchia 2015). The latter is measured through their Lyman Continuum escape fractions (f_{esc}(Ly C)), defined as the ratio between the H-ionizing radiation that is emitted intrinsically, and that which reaches the IGM. In order for galaxies to account for the reionization of the Universe, either a significant average f_{esc} value is required ($f_{esc} = 10$–20 per cent; Ouchi et al. 2009; Robertson et al. 2013, 2015; Finkelstein et al. 2019; Naidu et al. 2020), or a high ionizing photon production efficiency. These ranges of f_{esc} have been observed for individual star-forming galaxies at $z \lesssim 4$ (e.g. Borthakur et al. 2014; Bian et al. 2017; Vanzella et al. 2018; Izotov et al. 2021), but not usually in large numbers (Leitet et al. 2013; Leitherer et al. 2016; Steidel et al. 2018; Flury et al. 2022). An alternative to high escape fractions is a high ionizing photon production efficiency (ξ_{ion}), given by the ratio between the rate of ionizing photons being emitted ($\dot{n}_{ion}$), and the monochromatic non-ionizing ultra-violet (UV) luminosity density. Indeed, observational studies up to $z \sim 9$ have found ξ_{ion} to increase as a function of redshift (e.g. Endsley et al. 2021; Stefanon et al. 2022; Atek et al. 2024; Simmonds et al. 2023; Tang et al. 2023; Harshan et al. 2024; Pahl et al. 2024; Saxena et al. 2024; Simmonds et al. 2024a).

The behaviour of ξ_{ion} as a function of redshift has important consequences on the cosmic budget of reionization (e.g. Muñoz et al. 2024), defined as the number of ionizing photons produced per comoving volume unit of the Universe ($\dot{N}_{ion}$). Three ingredients must be provided in order to study $\dot{N}_{ion}$: (1) a prescription for f_{esc}, (2) a UV luminosity density function, ρ_{UV}, describing the number of galaxies per unit volume that have a given UV luminosity, as a function of redshift (e.g. Bouwens et al. 2021; Adams et al. 2024; Donnan et al. 2024; Robertson et al. 2024, Whitler et al., in preparation), and (3) constraints on ξ_{ion}. In addition, the IGM clumping factor of the Universe has to be considered (e.g. Madau, Haardt & Rees 1999; Kaurov & Gnedin 2014; So et al. 2014). This factor is a measure of the uniformity of the matter distribution in the Universe, and has crucial implications on reionization since it relates to the amount of atomic recombinations taking place in the IGM. Briefly, a higher clumping factor implies that more ionizing photons need to be emitted per unit volume at a given redshift in order to sustain hydrogen ionization.

Before the launch of the JWST (Gardner et al. 2023), it was common practice to set f_{esc} and ξ_{ion} as constants. Fortunately, the JWST has given us an unprecedented view of the early Universe at rest-frame optical wavelengths, which has allowed us to place better constraints on ξ_{ion}. In particular, Simmonds et al. (2024a) studied a sample of emission-line galaxies (ELGs) at $z \sim 4$–9 using photometry obtained with the Near Infrared Camera (NIRCam; Rieke et al. 2023), on board the JWST. The mean redshift of reionization is at $z = 7.68 \pm 0.79$ (Planck Collaboration VI 2020), meaning that this study (and the many others enabled by JWST) probe deep into the EoR. Through Hα and [O III] emission line fluxes, Simmonds et al.

(2024a) estimated ξ_{ion} for a sample of 677 galaxies. In parallel, they inferred the same quantity by using the spectral energy distribution (SED) fitting code `Prospector` (Johnson et al. 2019, 2021). They find that the ξ_{ion} measurements estimated by emission line fluxes agree with the values obtained by `Prospector`. Additionally, they conclude that ξ_{ion} increases with redshift, and that this increase is due to low-mass faint galaxies having more bursty star formation histories (SFHs). Here, burstiness is quantified by the ratio between recent (averaged over 10 Myr) and past (averaged over 100 Myr) star formation rates (SFRs), which is associated with low stellar masses (Weisz et al. 2012; Guo et al. 2016; Looser et al. 2023a), mainly due to the increased importance of stellar feedback. At high redshifts, however, burstiness can also be explained by the imbalance between gas accretion and supernovae (SNe) feedback time-scales, which prevent star formation equilibrium in the ISM (Faucher-Giguère 2018; Tacchella, Forbes & Caplar 2020). We note that the SFR_{10}/SFR_{100} ratio is a direct measure of the recent SFH, and its variance for an ensemble of galaxies measures short-term star formation variability ('burstiness'; Caplar & Tacchella 2019).

The sample constructed in Simmonds et al. (2024a) suffered from one main limitation: since emission lines were required, and with a sufficient strength so that they were measurable from photometry, this sample was biased towards star-forming galaxies with significant Hα and/or [O III] emission. In fact, Laseter et al. (in preparation) demonstrate ξ_{ion} is consistently high ($\log(\xi_{ion}/[\mathrm{Hz\ erg}^{-1}]) \approx 25.5$) down to [O III] equivalent widths of 200Å due to low metallicities ($Z \lesssim 1/10Z_{\odot}$), further demonstrating this bias from the past results. Given the agreement found between `Prospector` and the emission line measurements of ξ_{ion}, in this work, we use `Prospector` to fit the full JWST Advanced Deep Extragalactic Survey (JADES; Bunker et al. 2024; Eisenstein et al. 2023a) photometry set for a sample of JADES galaxies in the Great Observatories Origins Deeps Survey South (GOODS-S; Giavalisco et al. 2004). Our sample is 90 per cent complete in stellar mass down to masses of $\log(M_{\star}/[M_{\odot}]) \sim 7.5$, providing us a deep statistical view of the ionizing properties of galaxies.

The structure of this paper is the following. In Section 2, we present the data used in this work, along with the sample selection criteria. In Section 3, we present our `Prospector` fitting method. Some general properties of the sample are given in Section 4, followed by our constraints on the ionizing properties of galaxies in Section 5. Implications for reionization are discussed in Section 6, while the caveats and limitations of our methods are discussed in Section 7. Finally, brief conclusions are presented in Section 8. Throughout this work we assume $\Omega_0 = 0.315$ and $H_0 = 67.4\,\mathrm{km\,s^{-1}\,Mpc^{-1}}$, following Planck Collaboration VI (2020).

2 DATA AND SELECTION CRITERIA

In this section, we describe the data and selection criteria applied to build our sample of galaxies, with the goal to construct a stellar mass complete sample between redshifts 3 and 9.

2.1 Data

We use the full JADES (Bunker et al. 2024; Eisenstein et al. 2023a) photometry set in the GOODS-S region, including the publicly available NIRCam Deep imaging (Rieke et al. 2023), and the JADES Origins Field (JOF; Eisenstein et al. 2023b), covering an area of $\sim 45\,\mathrm{arcmin}^2$ with an average exposure time of 130 h. When available, we also use photometry from the JWST Extragalactic Medium-band Survey (JEMS; Williams et al. 2023), and from the
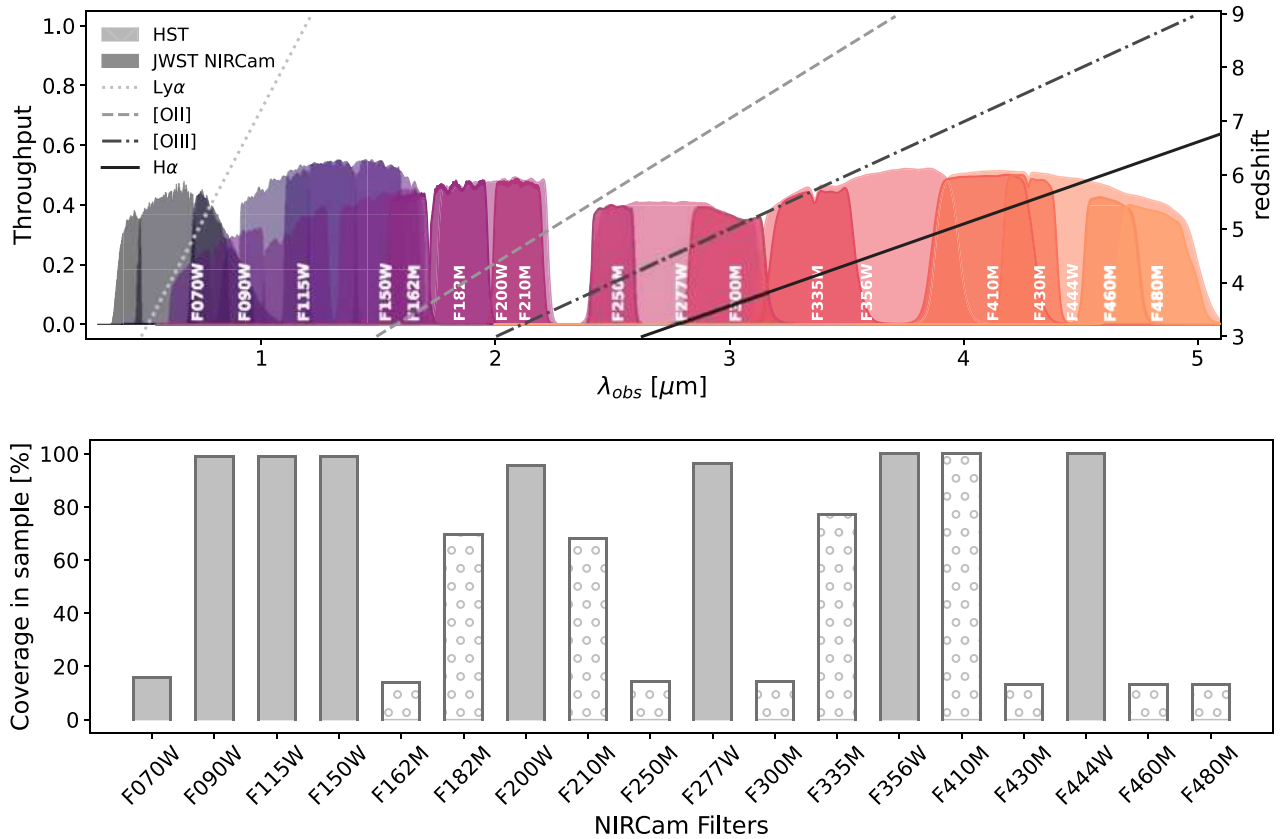
Figure 1. *Top panel:* Throughputs of the HST and NIRCam filters used in the SED fitting in this work for galaxies at $3 \le z_{phot} \le 9$. It is important to note that not all of these filters are available for every galaxy studied in this work. The hatched areas show the HST ACS bands: F435W, F606W, F775W, F814W, F850LP, and the HST IR bands: F105W, F125W, F140W, and F160W. While the filled regions are labelled and show the JWST NIRCam bands, from left to right: F070W, F090W, F115W, F150W, F162M, F182M, F200W, F210M, F250M, F277W, F300M, F335M, F356W, F410M, F430M, F444W, F460M, and F480M. The lines show the observed wavelengths of selected emission lines (Ly α, [O II], [O III], and Hα) with redshift. *Bottom panel:* percentage of sources in our final, stellar mass-complete sample that are covered by each JWST NIRCam filter. The medium bands are shown as dotted areas.

First Reionization Epoch Spectroscopic Complete Survey (FRESCO; Oesch et al. 2023).

2.1.1 Photometry

The photometric catalogue used in this work has been produced in the same way as the one used in Simmonds et al. (2024a). In brief, the source detection and photometry leverage both the JEMS NIRCam medium band and JADES NIRCam broad and medium band imaging. Detection was performed using the PHOTUTILS (Bradley et al. 2022) software package, identifying sources with contiguous regions of the SNR mosaic with signal $> 3\sigma$ and five or more contiguous pixels. We also use PHOTUTILS to perform circular aperture photometry with filter-dependent aperture corrections based on model point-spread-functions following the method of Ji et al. (2024), as described in Robertson et al. (2024). In addition to the NIRCam observations, *HST* images from the Hubble Legacy Field programme (Illingworth et al. 2016; Whitaker et al. 2019), and the Cosmic Assembly Near-Infrared Deep Extragalactic Legacy Survey (CANDELS; Grogin et al. 2011; Koekemoer et al. 2011), as well as reductions of GOODS-S from Giavalisco et al. (2004), are used. The details of the catalogue generation and photometry will be presented in Robertson et al. (in preparation). In this work, we use a Kron aperture placed on images that have been convolved to a common resolution, and impose an error floor of 5 per cent in each band. Our photometry does not take

include the EAZY derived photometric offsets, however, we find that the NIRCam photometric offsets are small given the uncertainty of the photometry (see Appendix A). The throughputs of the filters used in this work are shown in Fig. 1, as well as emission lines of interest and how their observed wavelength evolves with redshift.

2.1.2 Redshifts

Due to the richness of the photometry set, photometric redshifts (z_{phot}) can be obtained with great accuracy (Hainline et al. 2024). When fitting SEDs in this work, we use the z_{phot} inferred by the template-fitting code EAZY (Brammer, van Dokkum & Coppi 2008), as described in Hainline et al. (2024) and Rieke et al. (2023). Additionally, when available, we make use of spectroscopic redshifts (z_{spec}) from the Near-Infrared Spectrograph (NIRSpec; Jakobsen et al. 2022), as well as those reported in literature (Puskás et al. in preparation), including the JADES NIRSpec redshifts from Bunker et al. (2024) and D'Eugenio et al. (2024). In particular, they have been compiled from the Atacama Large Millimeter/submillimeter Array (ALMA) Spectroscopic Survey in the Hubble Ultra-Deep Field (ASPECS; Walter et al. 2016), CANDELS (Grogin et al. 2011), the 3D-Hubble Space Telescope (*HST*) Survey (Momcheva et al. 2016), the Multi Unit Spectroscopic Explorer (MUSE; Bacon et al. 2010) Ultra-Deep Field DR2 (Bacon et al. 2023), and a redshift catalogue (F. Sun private communication) produced from grism data of the

First Reionization Epoch Spectroscopic Complete Survey (FRESCO; Oesch et al. 2023).

We selected galaxies that were matched to JADES NIRCam positions within 0.25 arcsec, and that were flagged as reliable by each team. Since galaxies often have multiple z_{spec} measurements, we defined four categories to collate the several redshift measurements into one, which we call z_{best}:

(i) **Category A:** Only one redshift labelled as having the highest quality. We use this redshift as z_{best}.

(ii) **Category B:** Multiple redshifts with the same (highest) quality that agree when rounded to the second decimal. We use this rounded value as z_{best}.

(iii) **Category C:** Multiple solutions with the same (highest) quality that have a non-dramatic disagreement (with a difference smaller than 1). We define z_{best} as the mean between the solutions and add errors reflecting the difference.

(iv) **Category D:** Multiple solutions with the same (highest) quality that have a dramatic disagreement ($\Delta > 1$). In these cases, we keep all the highest quality redshifts and follow up with a visual inspection.

2.2 Sample selection criteria

In order to build a sample as complete as possible, we only impose two conditions that have to be met: (1) an S/N of at least 3 in the F444W band, and (2) redshifts $3 \leq z \leq 9$. Based on the nature of the redshift used (photometric or spectroscopic), we construct two samples, that we now introduce.

The photometric sample is initially composed of 37 272 galaxies. We use the SED fitting code PROSPECTOR (Johnson et al. 2019, 2021) to fit the full sample (see Section 3), yielding a total sample of 35 442 galaxies. The cases that failed (~ 5 per cent) were due to either poor photometric coverage (< 6 NIRCam photometric points) or to them being false detections (e.g. a diffraction spike). In order to have reliable inferred galaxy properties, we only use the results which have a reduced $\chi^2 \leq 1$, resulting in a final photometric sample with 25 319 galaxies. The completeness in stellar mass and UV magnitude is discussed in Section 4. We note that if we extend the limit up to $\chi^2 = 10$, we obtain 29 323 galaxies instead. However, the final stellar mass complete sample is virtually unchanged from the one discussed in this work. The spectroscopic sample is composed of 1620 galaxies, all of which are also part of the photometric sample. Their redshift classification is as follows: 1234 in Category A, 363 in category B, 12 in category C, and 11 in category D.

3 SED FITTING WITH PROSPECTOR

As demonstrated in Simmonds et al. (2024a), the ionizing properties inferred with the SED fitting code PROSPECTOR (Johnson et al. 2019, 2021) are in good agreement with those obtained by emission line fluxes, when such fluxes are detected. Therefore, in this work, we fit the entirety of our samples with PROSPECTOR, without introducing an additional selection bias (i.e. by only selecting emission line galaxies).

PROSPECTOR uses photometry and/or spectroscopy as an input in order to infer stellar population parameters, from UV to IR wavelengths. We use photometry from the *HST* ACS bands: F435W, F606W, F775W, F814W, F850LP, and from the HST IR bands: F105W, F125W, F140W, and F160W. In addition, we use the JADES NIRCam photometry from: F090W, F115W, F150W, F162M, F200W, F250M, F277W, F300M, F335M, F356W, F410M, and F444W. Finally, when available, we include JEMS photometry: F182M, F210M, F430M, F460M, and F480M. The same Kron convolved aperture is used to extract the HST, JADES and JEMS photometry.

For the photometric redshift sample, we adopt a clipped normal distribution using the EAZY z_{phot} as the redshift mean, with the sigma given by the z_{phot} errors. Whereas for the spectroscopic redshift sample we fix the redshift to z_{spec} for galaxies in Categories A, B, and D, and use the same prior as for the photometric sample for galaxies in Category C.

We vary the dust attenuation and stellar population properties following Tacchella et al. (2022a). In summary, we use a two-component dust model described in Charlot & Fall (2000) and Conroy, Gunn & White (2009). This model accounts for the differential effect of dust on young stars (< 10 Myr) and nebular emission lines, through different optical depths and a variable dust index (Kriek & Conroy 2013). We adopt a Chabrier (Chabrier 2003) initial mass function (IMF), with mass cutoffs of 0.1 and 100 $M_\odot$, respectively, allowing the stellar metallicity to explore a range between 0.01–1 $Z_\odot$, and include nebular emission. The continuum and emission properties of the SEDs are provided by the Flexible Stellar Population Synthesis (FSPS) code (Byler et al. 2017), based on CLOUDY models (v.13.03; Ferland et al. 2013) using MESA Isochrones & Stellar Tracks (MIST; Choi et al. 2016; Dotter 2016), and the MILES stellar library (Vazdekis et al. 2015). We note that he UV extension of the MILES library is based on the Basel Stellar Library (BaSeL; Lastennet et al. 2002). These CLOUDY grids introduce an upper limit on the permitted ionization parameters ($\log \langle U \rangle_{max} = -1.0$). We briefly remark here that this upper limit might not be appropriate for high-redshift galaxies (see e.g, Cameron et al. 2023). Due to the stochastic nature of the IGM absorption, we set a flexible IGM model based on a scaling of the Madau model (Madau 1995), with the scaling left as a free parameter with a clipped normal prior ($\mu = 1.0, \sigma = 0.3$, in a range [0.0, 2.0]). Last but not least, we use a non-parametric SFH (continuity SFH; Leja et al. 2019). This model describes the SFH as eight different SFR bins, the ratios and amplitudes between them are in turn, controlled by the bursty-continuity prior (Tacchella et al. 2022b). For a general view of the goodness of fits of our stellar mass complete sample (described in Section 4.2), we direct the reader to Appendix A, where we show a comparison between the modelled and observed photometry, as a function of the bands being used.

Fig. 2 shows example SEDs and best-fitting spectra for our sample. From top to bottom the redshift increases from 3.5 to 8.5, as indicated on the top left of each panel. The markers show *HST* (triangles) and JWST NIRCam (circles) photometry with their corresponding errors. The purple shaded area corresponds to the rest-frame spectral region at $\lambda_{rest-frame} = 1250$–2500 Å, used to estimate the rest-frame UV continuum slope (β; Calzetti, Kinney & Storchi-Bergmann 1994), defined as $F_\lambda \propto \lambda^\beta$. We obtain β by fitting a line to the best-fit SED provided by PROSPECTOR. We stress that there are important limitations to the measurements of β without spectra (for a full review, see Austin et al. 2024). Finally, the vertical dashed lines show the observed wavelength of Ly α, [O II], [O III], and H α. We note that not all galaxies have obvious emission lines detected in their photometry, illustrating the advantage of our sample selection (see for example, the second panel: JADES-GS $+ 53.06045 - 27.82581$).

4 SAMPLE GENERAL PROPERTIES

In this section, we discuss some of the general properties of our samples. We first compare the photometric redshifts inferred by EAZY
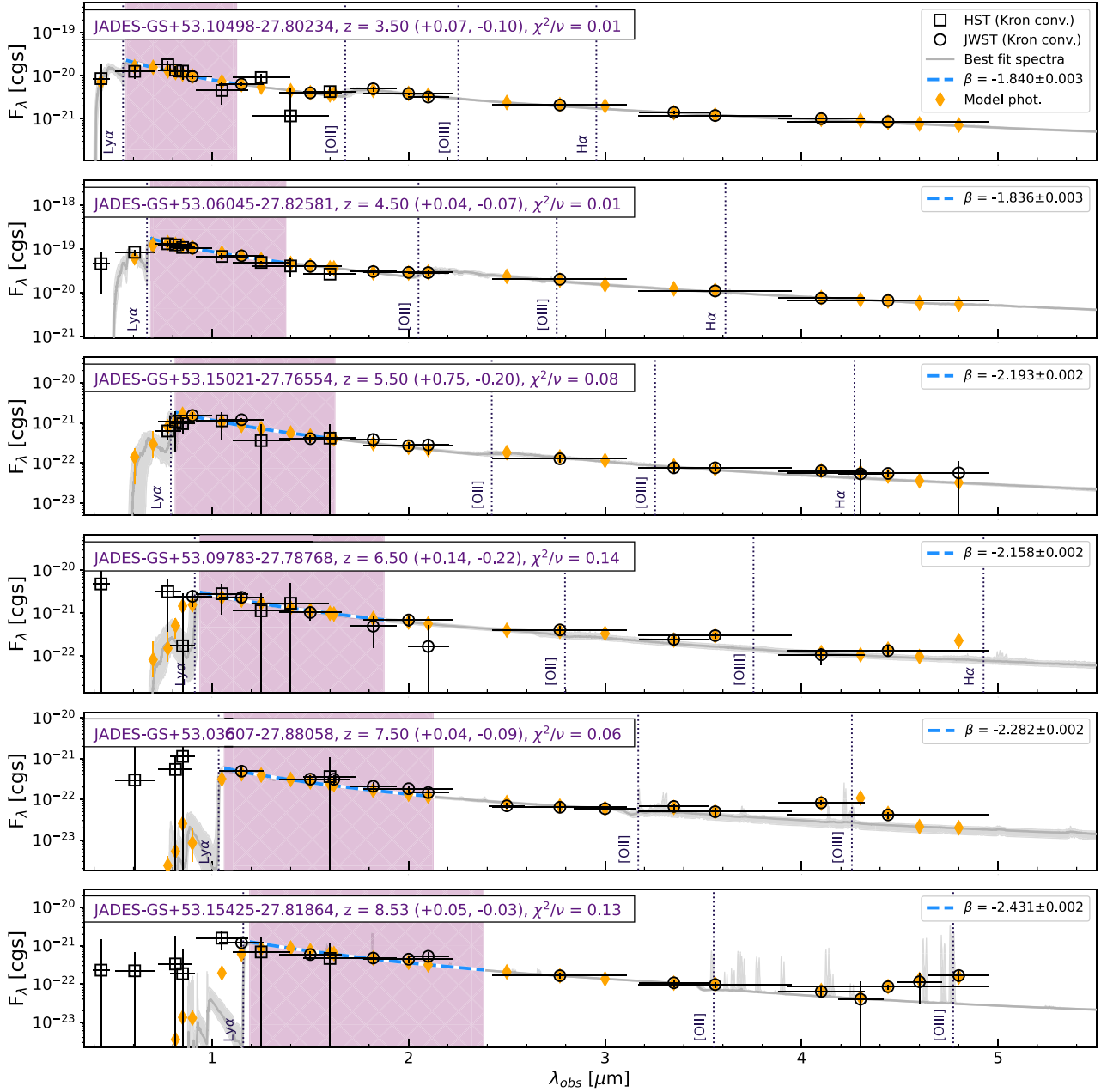
Figure 2. Representative example SEDs and best-fitting spectra for galaxies in our sample, assuming a continuity (i.e. non-parametric) SFH. From top to bottom the redshift increases from $z = 3.5$ to 8.5, in steps of 1, the galaxy identifiers, along with their z_{phot} and reduced χ^2 (for the JWST NIRCam photometry), are shown in the top left corner of each panel. The symbols show the photometric points for *HST* (open squares), JWST NIRCam (open circles), and model photometry (orange diamonds), respectively. The grey curves show the best-fitting spectra obtained by PROSPECTOR, with the spectral region used to estimate UV continuum slope (β; $\lambda_{rest-frame} = 1250$–$2500$ Å) shaded in purple. The observed wavelengths of Lyα, [O II], [O III], and Hα are shown as vertical dotted lines.

to those obtained with PROSPECTOR, and to the spectroscopic redshifts (when available). We then describe the stellar mass completeness of our sample.

4.1 Redshift comparisons

As previously mentioned, we use EAZY-inferred redshifts as priors when fitting the photometric sample. The redshifts obtained by this template-fitting tool have proven to be reliable when using the full JADES NIRCam photometry set (see fig. 13 of Rieke

et al. 2023). In Fig. 3, we compare the EAZY and the PROSPECTOR redshifts for the photometric sample. The PROSPECTOR redshifts are better constrained, as seen by the median error bars (black point). This is not surprising since PROSPECTOR is already using the EAZY results as a prior on the redshift. We note that PROSPECTOR is more flexible than EAZY, since the latter uses a fixed set of templates. Although, we note that the linear combination of templates used by EAZY might be outside of the PROSPECTOR parameter space, or disfavoured by the SFH or other PROSPECTOR priors. It can also be seen that a lower-redshift solution is preferred for several
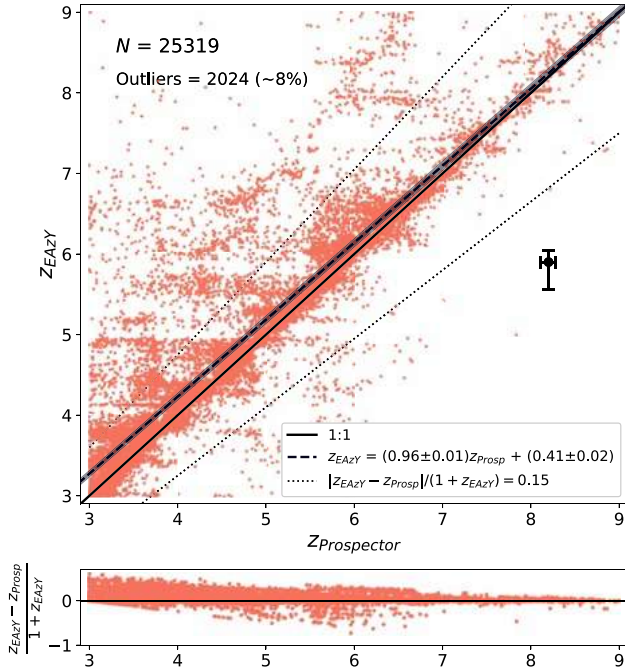
Figure 3. Comparison of input and output photometric redshifts. The vertical axis shows the photometric redshifts inferred using EAZY. These redshifts were used as priors in the SED fitting with PROSPECTOR, the medians of these posteriors are shown in the horizontal axis. The black point shows the redshift median errors, we note that the PROSPECTOR-inferred values tend to be better constrained, but that they overall follow a one-to-one trend with those inferred using EAZY, as can be seen by the best-fitting line (dashed black line). The points that fall outside of the dotted black lines are considered catastrophic outliers, there are 2036 galaxies that fall into this category, corresponding to ~ 8 per cent. We note that the outlier fraction is estimated by comparing the median values inferred by EAZY and PROSPECTOR. The former has considerably larger error bars in general.

sources. However, the distribution overall follows a one-to-one relation with a best-fitting slope of 0.96 ± 0.01 (black dashed line), demonstrating that both methods are in general agreement. We note that the number of sources decreases significantly as a function of photometric redshift: 10 215 at $3 \leq z < 4$, 6005 at $4 \leq 5$, 5203 at $5 < z \leq 6$, 3037 at $6 < z \leq 7$, 651 at $7 < z \leq 8$, and, 208 at $8 < z \leq 9$.

In order to test how well the z_{phot} retrieve real (z_{spec}) redshifts, in Fig. 4, we compare the photometric redshifts (from both EAZY and PROSPECTOR) to the spectroscopic sample in Categories A and B. The spectroscopic sample is biased towards brighter galaxies with stronger emission lines, compared to the full photometric sample, so we would expect more accurate z_{phot} estimations. We find a good agreement between z_{phot} and z_{spec} (i.e. $|z_{spec} - z_{phot}| < 0.15$), with only a small fraction of outliers. Specifically, 44 (35) for PROSPECTOR (EAZY) derived redshifts, corresponding to $\sim 3.1\%$ ($\sim 2.5\%$) of the subsample, where photometry alone makes it hard to distinguish a spectral break from another. From this comparison, we cannot say if one code performs better than the other, but we can conclude that both retrieve the correct redshift in the majority of the cases. We highlight that the SED modelling uncertainties and redshift variations are self-consistent.

Given the agreement between z_{phot} and z_{spec}, in the remainder of this work, we use the photometric sample unless explicitly stated.
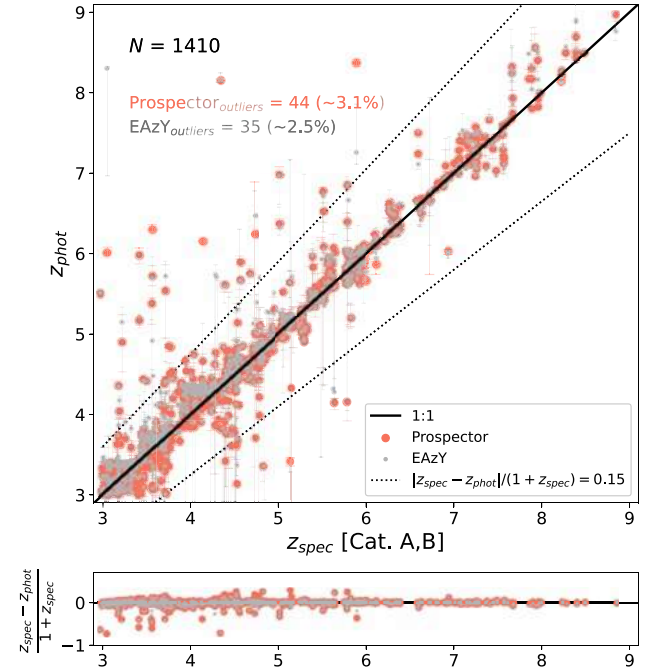

Figure 4. Comparison of photometric and spectroscopic redshifts, when spectroscopic redshifts in category A and/or B are available. Both PROSPECTOR (larger orange circles) and EAZY (smaller grey circles) inferred values generally follow a one-to-one relation with the spectroscopic redshifts, with some exceptions. We conclude that both codes can retrieve z_{spec} successfully in the majority of cases. The points that fall outside of the area delimited by the dotted lines are considered catastrophic outliers. There are 44 (35) of such objects inferred by PROSPECTOR (EAZY), corresponding to ~ 3.1 per cent (~ 2.5 per cent) of the subsample with spectroscopic redshifts in categories A and B.

4.2 Completeness of sample

To estimate the stellar mass completeness of our sample, we use the redshifts and stellar masses inferred with PROSPECTOR, noting that the spectroscopic sample overlaps with the photometric one, and that the redshifts are in tight agreement. A corner plot showing the mean shape of the posteriors for these parameters can be found in Appendix B.

To assess the 90 per cent stellar mass completeness limit of our photometric sample, we follow the procedure described in section 5.2 of Pozzetti et al. (2010). In summary, for every redshift, we define a minimum mass (M_{min}), above which all types of galaxies can potentially be observed. To obtain M_{min}, we first need to calculate the limiting stellar mass (M_{lim}) for each galaxy, given by:

$$\log(M_{lim}) = \log(M_\star) + 0.4(m - m_{lim}), \tag{1}$$

where $M_\star$ is stellar mass in units of solar masses. M_{lim} represents the mass a galaxy would have if its apparent magnitude (m) were equal to the limiting magnitude of the survey (m_{lim}) in the F444W band. This band was chosen since it has the longest effective wavelength, and thus, is the tracer of stellar mass. We divide our data into three depths depending on the exposure time: medium ($T_{exp} < 25$ ks), deep (25 ks $\leq T_{exp} < 65$ ks), and ultra-deep ($T_{exp} > 65$ ks), with 5σ flux depths of 6, 4.5, and 2.65 nJy, respectively. Once M_{lim} has been calculated for every galaxy, we compute M_{min} for each field by selecting the faintest 20 per cent of the galaxies with a given T_{exp}, and finding the limit above which 90 per cent of the selected M_{lim} values lie. Fig. 5 shows the stellar mass of our sample as a function of redshift (grey